Near-Field Measurement and Calibration Technique for RF EMF Exposure Assessment of mm-wave 5G Devices

Lundgren, Johan; Helander, Jakob; Gustafsson, Mats; Sjöberg, Daniel; Xu, Bo; Colombi, Davide

2019

CODEN:LUTEDX/(TEAT-7267)/1-27/(2019)

Near-Field Measurement and Calibration Technique for RF EMF Exposure Assessment of mm-wave 5G Devices

Johan Lundgren, Jakob Helander, Mats Gustafsson, Daniel Sjöberg, Bo Xu, and Davide Colombi

Electromagnetic Theory
Department of Electrical and Information Technology
Lund University
Sweden

(TEAT-7267)/1-27/(2019): Johan Lundgren, et al, Near-Field Measurement and Calibration Technique for mm-wave 5G Devices

Johan Lundgren, Jakob Helander, Mats Gustafsson, and Daniel Sjöberg
johan.lundgren@eit.lth.se, jakob.helander@eit.lth.se,
mats.gustafsson@eit.lth.se, daniel.sjoberg@eit.lth.se

Department of Electrical and Information Technology, Electromagnetic Theory
Lund University,
P.O. Box 118, SE-221 00 Lund, Sweden

Bo Xu and Davide Colombi
bo.xu@ericsson.com, davide.colombi@ericsson.com

Ericsson Research, Ericsson AB, Stockholm, Sweden

This is an author produced preprint version as part of a technical report series from the Electromagnetic Theory group at Lund University, Sweden. Homepage `http://www.eit.lth.se/teat`

Editor: Mats Gustafsson

Abstract

Accurate and efficient measurement techniques are needed for exposure assessment of 5G portable devices—which are expected to utilize frequencies beyond 6 GHz—with respect to the radio frequency electromagnetic field exposure limits. Above 6 GHz, these limits are expressed in terms of the incident power density, thus requiring that the electromagnetic fields need to be evaluated with high precision in close vicinity to the device under test (DUT), i.e., in the near-field region of the radiating antenna. This work presents a cutting-edge near-field measurement technique suited for these needs. The technique—based on source reconstruction on a predefined surface representing the radiating aperture of the antenna—requires two sets of measurements; one of the DUT, and one of a small aperture. This second measurement functions as a calibration of both the measurement probe impact on the received signal, and the experimental setup in terms of the relative distance between the probe and the DUT. Results are presented for a 28 GHz and a 60 GHz antenna array; both developed for 5G applications. The computed power density agrees well with simulations at evaluation planes residing as close as one fifth of a wavelength ($\lambda/5$) away from the DUT.

1 Introduction

Mobile communication systems play a large role in today's interconnected world and the amount of mobile data traffic is constantly increasing. Between the fall of 2016 and 2017, the total data traffic in mobile networks increased by 65 % [15]. The next generation of wireless access systems (5G) plays an integral role for handling the future demands on traffic capacity; and to support the increasing data rates, a plausible solution has emerged that involves exploiting the larger bandwidths (which directly translates to a capacity increase) available at frequencies above 6 GHz. Moreover, 5G systems are expected to operate within several bands comprising frequencies below 6 GHz—where the conventional bands in use today lie—up to over 100 GHz [9]. Full system trials of 5G are ongoing and commercial networks are expected already in 2019. Much focus is given to the frequencies between 6–60 GHz and a substantial amount of research is devoted to the development of mobile devices operating in this frequency range.

Several different techniques for compliance measurements exist [1]. Depending on the frequency of interest combined with the proximity of the device under test (DUT), different regions of the electromagnetic field (EMF) dominate [24]. For frequencies below 6 GHz, the EMF compliance is assessed using specific absorption rate (SAR) and for frequencies above 6 GHz power density is utilized [16]—with limits for localized exposure generally taken as an average over a predefined area, *e.g.*, 4 cm^2 [10]. An overview of radio frequency (RF) EMF compliance assessment procedures and measurement techniques applicable above 6 GHz for incident power density is provided in IEC TR 63170[17].

One well-established measurement technique is based on amplitude measurement of the electric field components [21]. The method makes use of a miniaturized diode-loaded probe (see *e.g.*, Schmid and Partner Engineering AG [23]) to scan the field at sub-wavelength distances ($< \lambda$) from the device. An estimate of the phase, which cannot be directly measured by means of such probes, is obtained by using a plane-to-plane reconstruction algorithm. This requires the amplitude of the field to be scanned on two parallel planes at different distances from the source. The power density is then reconstructed by estimating the phase based on the measured amplitude of the electric field only. In addition, the field polarization ellipse is determined by rotating the probe at different angles. Although the robustness of such algorithms has been carefully validated numerically and experimentally [21], phase retrieval represents a source of uncertainty which cannot be left out and that might vary depending on the distance from the closest scan plane to the DUT. Since retrieving the phase also requires the same scan of the electric field to be repeated on two parallel planes—in addition to rotating the probe at different angles for each measurement point—the measurement time might become exceedingly long. Other conventional measurement techniques that retrieve both amplitude and phase with non-ideal probes are problematic since even with probe calibration, the precise point in space that the measurement corresponds to is not well-defined. This leads to an error in positioning and consequently phase, thereby making it a difficult task to evaluate the power density at very close ranges to the DUT.

This work presents a measurement technique—based on amplitude and phase retrieval—for obtaining the power density at a given surface situated some arbitrary distance away from a DUT, using a reference measurement of a small aperture. Throughout this work, the term power density indicates the time-averaged, incident power density in a single spatial point at a single frequency. The technique is adapted here on antennas operating at the millimeter wave (mm-wave) frequencies 28 GHz and 60 GHz, and is based on two sets of measurements; one of the DUT, and one of a small aperture necessary to calibrate the complete measurement setup. The calibration measurement needs only to be conducted once and may be utilized for multiple DUTs, presuming the setup is not subject to substantial drifting over the complete measurement time frame. Fig. 1 shows the measurement procedure and setup; the calibration aperture is shown in Fig. 1a, and an example DUT is shown in Figs. 1c and 1d. With the measurement data retrieved and the calibration performed, numerical integral equation solvers are used to reconstruct equivalent currents on a predefined surface representing the DUT, and subsequently to compute the power density at any plane of interest. Three different DUTs were measured and compared with simulations.

The innovative calibration approach using the small aperture measurement has the substantial benefit of not only correcting for the receiving probe's impact on the measured signal, but also of handling the spatial alignment of the DUT relative to the scan plane. This second feature is essential when conducting RF EMF exposure tests at said frequencies, since the power density must be reconstructed in planes residing in the near-field region of the DUT. In accordance with the field's radial dependence in this region, a distance offset of *e.g.,* 1 mm (corresponding to $\lambda/5$

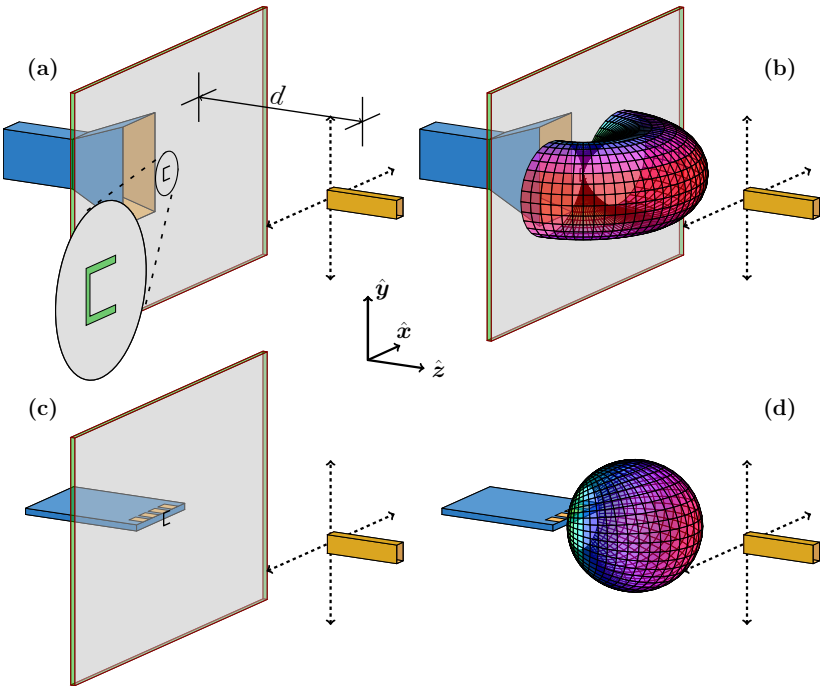

Figure 1: Schematic of the measurement procedure. **a**: A receiving probe is situated in the center of a planar measurement surface, a distance d away from a small aperture in a finite metallic plane. A transmitting antenna is positioned on the other side of the metallic plane. A high gain broadside antenna is preferable to ensure sufficient power flow through the aperture, although in theory nothing prohibits the usage of the DUT itself. **b**: The transmitting antenna excites the aperture which then radiates as a dipole. The reference measurement is conducted by sampling the fields in a discretized grid across the measurement surface using the receiving probe. **c**: The transmitting antenna is removed, and the DUT is aligned with respect to the previous position of the aperture. **d**: A second measurement is conducted on the DUT, and the field is sampled in the same grid as before.

at 60 GHz) would result in a substantial change in both the amplitude and phase of the reconstructed radiated electromagnetic fields. The small aperture calibration measurement suppresses this margin of error as the setup is calibrated to the specific distance.

The paper is organized as follows. The next section presents results from two measurement campaigns conducted at 28 GHz and 60 GHz of two antenna arrays developed for 5G applications, and a benchmark case of a 60 GHz standard gain horn antenna. Thereafter details regarding theory, measurement technique and post processing steps of the data are given. Then, a discussion of the results are presented, followed by conclusions, and, finally, information detailing the simulation settings and the measurement setup.

2 Results

Three different DUTs, shown in Figs. 2a–c, had their power density reconstructed from measurements of the near field using a single polarized, linearly polarized, probe. The DUT in Fig. 2a is a mobile phone mockup, capable of operating in the frequency region of 25-29 GHz, with four independently fed antennas. In this work we consider the operational frequency of 28 GHz. The cross polarization is low and the radiating elements are covered by a plastic chassis. A detailed description of the antenna array design can be found in [13]. A device of similar design was used for the development of the use cases described in IEC TR 63170 [17]. Two reconstruction planes were defined for this DUT, labeled plane 1 and 2, respectively, as shown in Fig. 2a. The second DUT is a linearly polarized 60 GHz patch array fed with a single transmission line with 3.3 % bandwidth[5], shown in Fig. 2b. It is mounted on a custom 3D printed stand with the transmission line bent over a rounded edge to reduce any unwanted radiation from the connector. The third DUT, shown in Fig. 2c, is a Flann $25240-20$ linearly polarized standard gain horn antenna operating between 49.9-75.8 GHz [11]. This DUT was measured at 60 GHz and selected as a benchmarking case due to its well-known radiation characteristics with high radiation efficiency, ease of modeling in commercial simulation software programs, and its high directivity, from which errors related to the measurement plane being finite are suppressed.

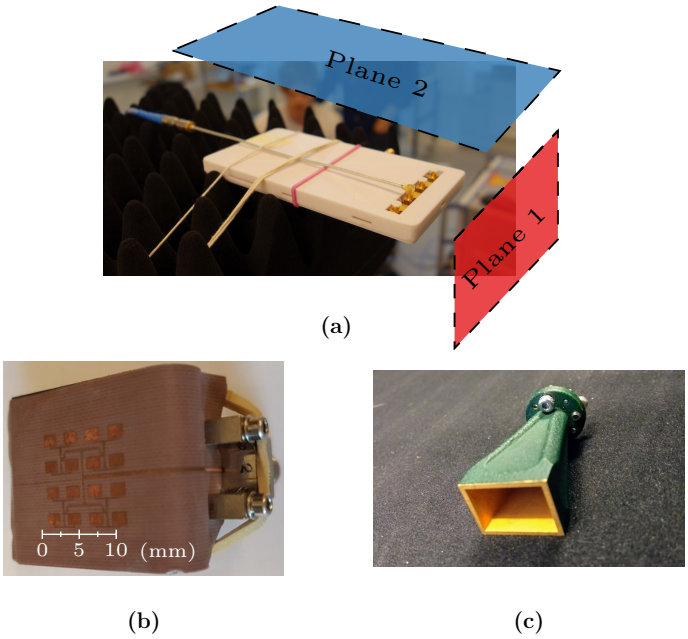

(a) (b) (c)

Figure 2: The DUTs used in this work. **a**: A mobile phone mockup from Sony Mobile operating at 28 GHz. **b**: A single feed 60 GHz linearly polarized patch array. **c**: A Flann $25240-20$ standard gain horn operating at 60 GHz.

Table 1: The relative difference between the measurement data set, x and the simulation data set, y for maximum spatial peak power density (numbers in parenthesis) and maximum spatially averaged power density. The averaging was carried out over a circular area of 4 cm^2, and each data set has been individually normalized to the same relative output power. The rows correspond to different data sets and the columns to different reconstruction distances.

	Relative difference of the maximum spatially averaged/(peak) power density $:= \lvert x-y \rvert / y$			
	1 mm	5 mm	10 mm	20mm
Horn (measured)	0.3 (0.7) %	2 (7) %	0.8 (2) %	-
Horn (synthetic)	0.8 (2) %	0.2 (7) %	2 (7) %	-
60 GHz Patch	1 (39) %	0.3 (15) %	3 (2) %	-
28 GHz Plane 1	-	10 (8) %	11 (12) %	15 (21) %
28 GHz Plane 2	-	34 (67) %	33 (50) %	28 (23) %

2.1 Measured Results

The mockup shown in Fig. 2a was measured by scanning a probe in a plane, parallel to the closest surface of the DUT, distanced $d = 60$ mm away, see Fig. 1. The power density was then reconstructed in planar surfaces distanced 5 mm, 10 mm and 20 mm away from the DUT, corresponding to the distances used in a the IEC TR 63170 28 GHz case study [17]. The mockup was simulated with the multilevel fast multipole method (MLFMM) using the electromagnetic (EM) simulation tool FEKO [2]. Due to the similarity of the results for the different port excitations, the results shown in Fig. 3 are limited to the excitation of the left uttermost port. Figs. 3a and 3b depict the comparison between measured and simulated results for plane 1 and 2, respectively, with no spatial averaging and on a 40 dB dynamic range. The simulated power densities are seen in the top of the figure and the power densities from reconstructing the fields from measured data is seen in the bottom of the figure.

The 60 GHz patch array antenna, Fig. 2b, was measured by a probe in a plane at a distance of 25 mm. The power density was calculated for the distances 1 mm, 5 mm and 10 mm. The antenna was simulated using the EM simulation tool CST. Similar to Fig. 3, a comparison between measured and simulated power density is shown in Fig. 4

As a verification of the technique presented in this paper a standard gain horn, shown in Fig. 2c, was measured at 60 GHz. The field was measured in a plane distanced 50 mm from the DUT. The normalized power density in the reconstruction planes distanced 1 mm, 5 mm, and 10 mm from the aperture of the standard gain horn is shown in Fig. 5. Results are shown for three different cases: 1) the direct full-wave simulation of the DUT in FEKO, 2) synthetic data, where simulated data was used as input (at the 50 mm distance) to the reconstruction routine, and 3)

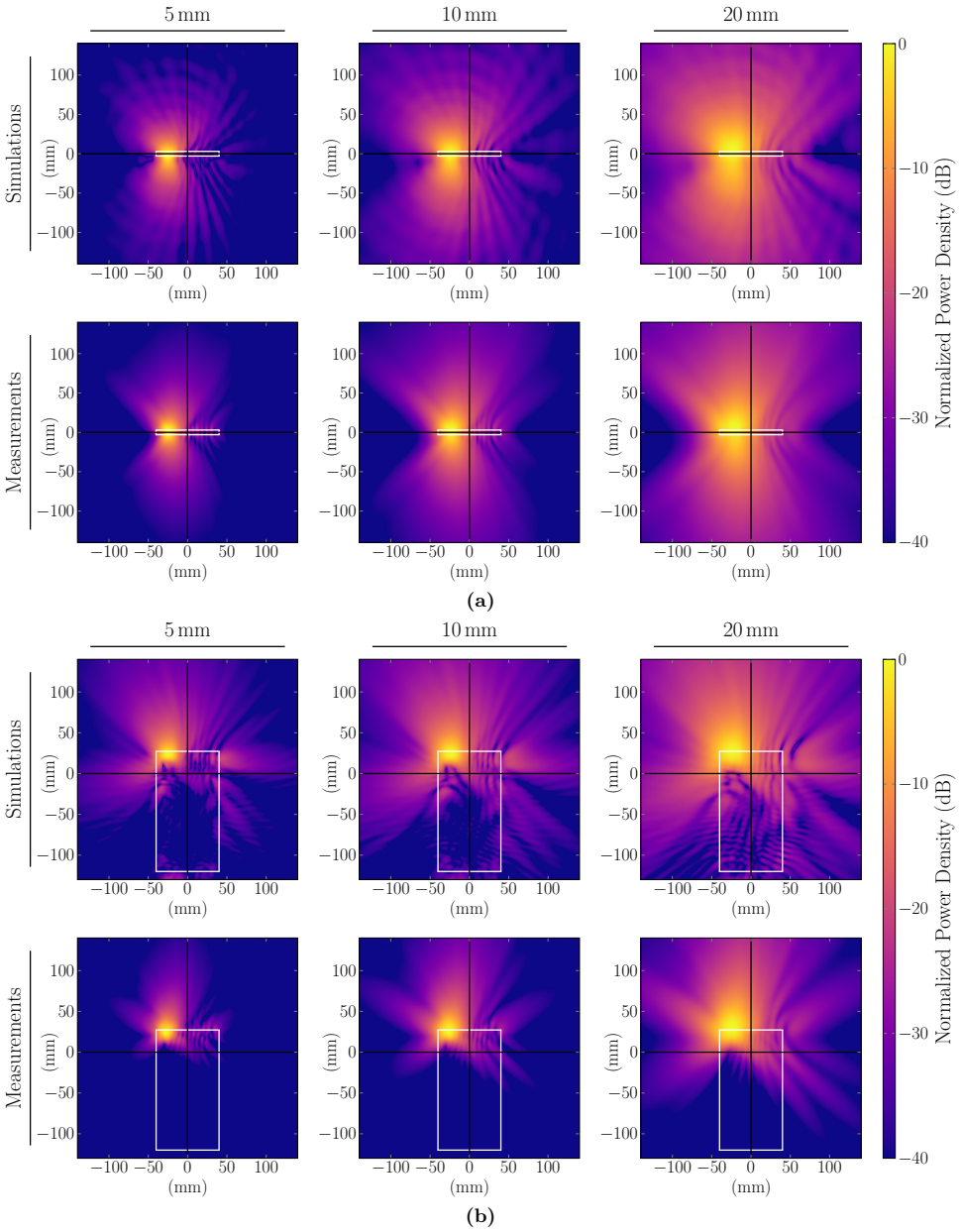

Figure 3: Normalized power density at 28 GHz in the reconstruction planes distanced 5 mm, 10 mm, and 20 mm (left to right) for the Sony Mobile phone mockup. Plane 1 is depicted in **a**, and plane 2 in **b**. The rows depict: full-wave simulations of the DUT in FEKO (top), and the results of the measurement data as input to the reconstruction technique (bottom). The white lines depict the outline of the DUT, and the black crosshair marks the mutual origin. The dynamic range of all plots is 40 dB.

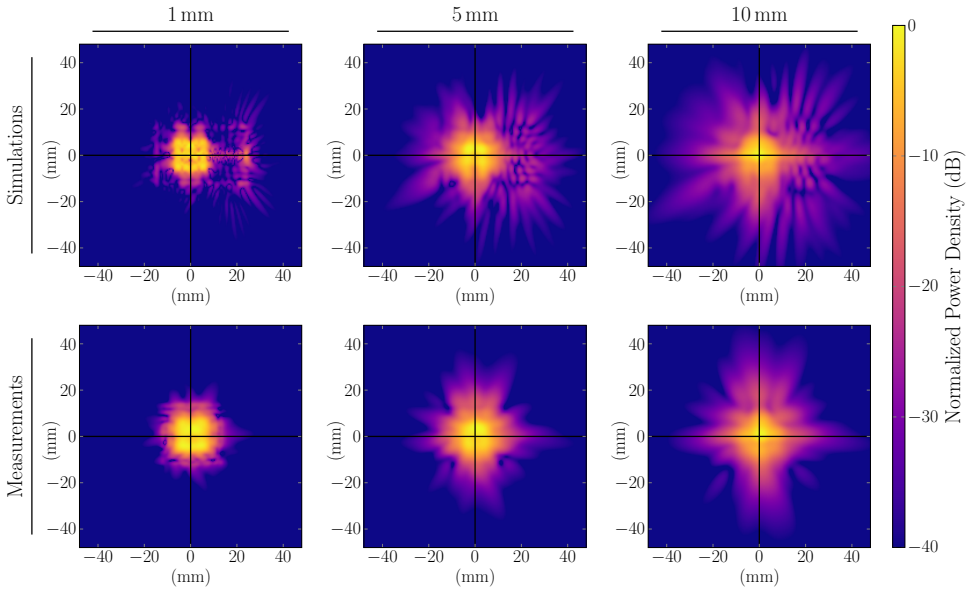

Figure 4: Normalized power density at 60 GHz in the reconstruction planes distanced 1 mm, 5 mm, and 10 mm (left to right) from the aperture of the patch array antenna. The rows depict: full-wave simulations of the DUT in CST (top), and the results of the measurement data as input to the reconstruction technique (bottom). The black crosshair marks the mutual origin. The dynamic range of all plots is 40 dB.

using measurement data as input to the reconstruction routine. Since the standard gain horn is a custom supplied antenna [11], it provides a benchmark case where all system losses and gains can be accounted for.

The maximum spatial peak incident power density was computed for the horn measurement, and at the plane distanced 10 mm away this value was 0.655 $\mathrm{W/m^2}$, 0.621 $\mathrm{W/m^2}$ and 0.656 $\mathrm{W/m^2}$ for the measurement data, synthetic data and simulation, respectively. A comparison of the maximum spatial peak power density for the three DUTs is presented as the numbers in parenthesis in Table 1. The results for all measured DUTs are compared to the respective simulationsin terms of the relative difference between the simulated maximum peak power density to the maximal value reconstructed from measurements. This table presents relative values and each reconstruction plane is normalized such that each power density value in a specific plane is divided by the total power density in that specific reconstructed/simulated plane, yielding a normalized power density of 1 in each plane, see Appendix F.

The results presented in Fig. 3-5 all show the power density, unaveraged. However, the power density averaged over a certain area is also of interest [10] and a comparison between the reconstructed fields and simulations in terms of spatially averaged power density is also seen in Table 1, numbers without parenthesis.The averaging area utilized was a circular area of 4 $\mathrm{cm^2}$ and other averaging areas are available in Appendix A.

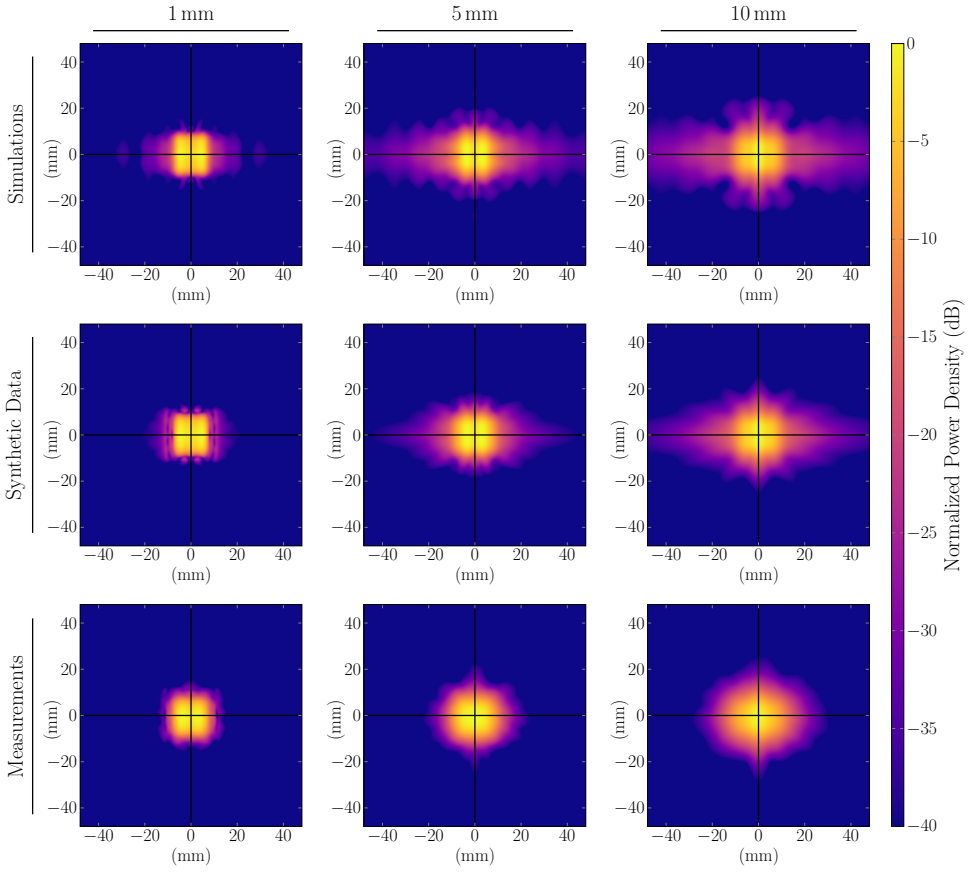

Figure 5: Normalized power density at 60 GHz in the reconstruction planes distanced 1 mm, 5 mm, and 10 mm (left to right) from the aperture of the standard gain horn. The rows depict: full-wave simulations of the DUT in FEKO (top), synthetic data where simulated data as an input to the reconstruction technique (center), and the results of the measurement data as input to the reconstruction technique (bottom). The black crosshair marks the mutual origin and the dynamic range of all plots is 40 dB.

2.2 Theory and Measurement Technique

A DUT in this work is a well functioning antenna, of arbitrary shape, radiating detectable power levels in a certain frequency interval in which the measurement is to be conducted. As disclosed in Fig. 1d, a radiating DUT is fixed at a certain position in space, and the emitted field is sampled on a surface some distance away from this DUT. It is well known that information regarding the field at other surfaces can be obtained from this measurement, and different techniques to realize this exist [3, 8, 20]. However, many of these rely on the use of well-defined measurement antennas (probes) and do not provide absolute positioning of the scanned plane in relation to the DUT, which is a necessity for accurately reconstructing the power density. This requirement on an absolute position between the DUT and the scan/measurement plane, originates from the goal to estimate the power density at sub-wavelength distances from the DUT. Any position error directly translates to large errors of the estimated power density since the electromagnetic fields have a strong radial dependence in close vicinity of the DUT.

In this work, we use a calibration method relying on a reference measurement of a small aperture in order to obtain accurate reconstruction of the radiated power density from a measured DUT. In essence, this is achieved by reconstructing the equivalent currents on a surface representing the radiating part of the DUT and thereafter calculating the corresponding radiated fields in the evaluation planes of interest using computational codes based on the method of moments (MoM), *i.e.*, numerical integral equation solvers. In summary, the technique is explained by the following steps:

1. Processing of raw measurement data.
2. Calibration, using measurement data of the small aperture, to remove the effects that the receiving probe has on the retrieved data, and to obtain a well-defined spatial position.
3. Reconstruction of equivalent currents on the surface of the DUT.
4. Computation of the electric and magnetic fields at a surface of interest from the reconstructed equivalent currents.
5. Calculation of the incident power density from the field in the previous step.

The rest of this section will focus on discussing these steps in more detail.

2.2.1 Measurement Data Processing

There is no inherent restriction on the shape of the measurement and reconstruction surfaces nor of the DUT. However, the DUTs presented in this work consist of radiating elements confined to a plane and a standard gain horn. Furthermore, only planar surfaces parallel to that of the radiating DUT are considered throughout this work, since this constitute an appropriate setting for the purpose of EMF exposure assessment. The first measured plane is that of the aperture as disclosed in Figs. 1a

and 1b. The aperture is then removed, and the DUT—aligned with respect to the previous position of the aperture—is measured in the same plane as the aperture was measured, see Figs. 1c and 1d. Samples of the transmitted signal are taken in discrete sampling points over the entire scan plane. The sampled data are extracted in order to retrieve the necessary field information in the following steps. The response is measured for several discrete frequency points in a given range $f_0 \pm \Delta f_0$. The frequency bandwidth, $2\Delta f_0$, enables the use of time gating procedures to suppress interactions with far away objects, and is specified as to realize a certain resolution of the signal in time domain [22]. Throughout this work Δf_0 was set to 2 GHz and 1 GHz for the 28 GHz and 60 GHz measurements, respectively. This provided more than adequate information to enable time gating procedures. Effects relating to choice of measurement bandwidth and frequency sampling can be further viewed in Appendix D.

2.2.2 Probe Correction Using an Electrically Small Aperture

Any given physical probe has a finite size and a non-local interaction with the electromagnetic field in its immediate surrounding. The probe is connected to a vector network analyzer (VNA) and the registered value in the receiving device is a complex-valued voltage signal accounting for the full probe interaction, rather than the complex-valued field in that particular discrete point of the finite aperture. This effect can be atoned for using probe correction techniques, of which there are several presented in classic literature [25]. These techniques calibrate for the interaction of the probe with the drawback of not having precise information on the position of that particular measurement point. Knowledge of the exact positioning of the system is vital, as the phase information is severely affected. Since the power density is computed from the electric and magnetic fields, a large uncertainty in the retrieved phase of the fields has a severe negative impact on the end result. In this work, a small aperture is measured as a reference measurement, see Fig. 1b, which allows for calibration of the probe and fixating the calibration to a well known physical position; that of the aperture. In turn, the position of the aperture acts as an alignment position once the DUT is inserted (Figs. 1c and 1d). This technique removes the need of delicate information regarding the probe and places that requirement on the aperture. As opposed to the probe, the aperture has a well-defined position from which the fields originate. This translates into obtaining measurements with a position put in relation to this well-defined point, removing the large uncertainty and phase error one would have obtained through traditional means of probe calibration.

Consider a small (compared to the wavelength of interest) aperture in a metal screen, see Fig. 1a. The aperture is designed preferably resonant to increase power flow through the aperture, although it is not required. Since the aperture is electrically small, its radiation characteristics is well-defined and of the first order; corresponding to that of a magnetic dipole [4]. It has a simple geometry that is easily modeled using numerical methods such as the MoM. The fields from this aperture at the measurement surface can be evaluated numerically utilizing any standard computational EM technique. These computed fields are then compared

to the measured signal to calibrate the setup. The calibration can be performed in many different ways including: determining the scattering matrix [12] of the measurement probe, using the reference measurement as the system Green function directly in the reconstruction algorithm, or as a simple point-wise division correcting the amplitude and phase of the measured signals. In this work, the latter was used and explained by considering the measured signals as an estimate of the co-polarized field value in the center of the probe.

In each discrete point, a correction term is obtained by normalizing the MoM simulation of the co-polarized component of the field from the aperture with the measurement of the aperture. These correction terms are then applied to the data of the measured DUT, and a probe corrected field with absolute positioning calibrated to the mathematical model used in the reconstruction algorithm is obtained. In this work only single polarized measurements were conducted; however, both polarizations can be incorporated by conducting a second set of measurements with a different orientation, *e.g.* a 90° rotation, of the probe [18].

The probe used for the 60 GHz measurements was an RFspin OEWG WR15, and a similar open-ended waveguide probe was used for the 28 GHz measurement.

2.2.3 Reconstruction of Equivalent Currents

The reconstruction of the sources is performed by expressing the solutions to Maxwell's equations using the electric field integral representation given by [14, 19]:

$$\boldsymbol{E}(\boldsymbol{r}) = \mathrm{j}k\eta_0 \int_S \boldsymbol{J}(\boldsymbol{r}')G(\boldsymbol{r}-\boldsymbol{r}') + \frac{1}{k^2}\nabla G(\boldsymbol{r}-\boldsymbol{r}')\nabla'\cdot\boldsymbol{J}(\boldsymbol{r}') + \boldsymbol{M}(\boldsymbol{r}')\times\nabla G(\boldsymbol{r}-\boldsymbol{r}')\,\mathrm{d}S', \quad (2.1)$$

where η_0 is the intrinsic impedance of free space, k is the free space wave number, G is the free space Green function, $\boldsymbol{J}$ and $\boldsymbol{M}$ are the electric and magnetic equivalent currents respectively that are positioned at $\boldsymbol{r}'$, S is the reconstruction surface and $\boldsymbol{r}$ is the position vector belonging to the measurement surface. $\boldsymbol{J}$ is needed if the problem is a half-space and $\boldsymbol{J}$ and $\boldsymbol{M}$ are needed for arbitrary geometries on the surface of the DUT. The computation of $\boldsymbol{J}$ given $\boldsymbol{E}$ is a type of problem arising in many scientific fields namely an inverse source problem [7], and it is mathematically ill-posed [12].

Numerically, the problem is addressed by defining an area representing the radiating aperture of the DUT. This area is discretized and (2.1) is reshaped into a matrix equation, using a suitable discretization method [6] as,

$$\boldsymbol{E} = \mathbf{N}^{\mathrm{e}}\boldsymbol{J} + \mathbf{N}^{\mathrm{m}}\boldsymbol{M}, \quad (2.2)$$

where $\boldsymbol{E}$ contains the measured component of the electric field in all spatial sampling points, $\boldsymbol{J}$ contains the spatially discretized currents on the reconstruction surface and the matrix operators $\mathbf{N}^{\mathrm{e}}$ and $\mathbf{N}^{\mathrm{m}}$ describe the mapping from $\boldsymbol{J}$ and $\boldsymbol{M}$ to $\boldsymbol{E}$ for two surfaces, thus it will differ depending on the chosen plane. For the rest of this work, we consider half-space geometries and use the field equivalence principle [4] to

reduce the problem to only electric currents $\boldsymbol{J}$ ($\boldsymbol{M}$ and $\mathbf{N}^{\mathrm{m}}$ in equation (2.2) are not present). As stated previously in Section 2.2.1, there is no requirement of planar measurement and reconstruction surfaces. However, utilization of such surfaces yields a decrease in computational time as very efficient numerical methods can be employed. The solution of (2.2) is ill-conditioned and a regularization procedure is required. A multitude of techniques exist to treat the regularization of such problems [12, 14] and we employ the truncated Singular Value Decomposition (SVD) method [12] and truncating when the singular values are lower than $0.1\sigma_{\max}$, where $\sigma_{\max}$ is the maximal singular value. This value was chosen for all presented data and further investigation of the singular values and choice of truncation is viewable in the Appendix C. The input data to equation (2.2) is the probe corrected measured field from the DUT and the output data are the equivalent currents on a predefined plane, in this case, the plane where the DUT is situated.

2.2.4 Fields from Equivalent Currents

With the equivalent currents reconstructed, equation (2.2) is executed to retrieve the electric field originating from these currents in any arbitrary evaluation surface after defining the appropriate matrix operator $\mathbf{N}^{\mathrm{e}}$ that describes the electric field integral representation for the new observation points. Similarly, the magnetic field is retrieved using the corresponding matrix form of the magnetic field integral representation.

2.2.5 Power Density Computation

The power density in a spatial reconstruction point $\boldsymbol{r}$ is given by

$$S_n(\boldsymbol{r}) = \frac{1}{2}\mathrm{Re}\{\boldsymbol{E}(\boldsymbol{r}) \times \boldsymbol{H}^*(\boldsymbol{r})\} \cdot \hat{\boldsymbol{n}}, \tag{2.3}$$

where the real part is denoted Re{}, $\boldsymbol{E}$ and $\boldsymbol{H}^*$ denote the electric field and the complex-conjugate of the magnetic field, respectively, $\times$ denotes the cross product, and $\hat{\boldsymbol{n}}$ denotes the unit vector normal to the evaluation surface. The power density is obtained once the full near-field measurement technique—including the previously mentioned processing steps—has been applied, and the measurement setup has been calibrated with respect to the total radiated power P_{r} (presuming all system gains and losses have been accounted for). A spatial average can subsequently be acquired through a convolution between the power density profile in the full reconstruction plane and the predefined averaging area.

3 Methods

3.1 Numerical Simulations

As the connectors are electrically large objects at 28 and 60 GHz they require enormous computational resources and were thus excluded from all simulations. The

28 GHz mockup was simulated in FEKO with the multilevel fast multipole method (MLFMM), and the microstrip feedlines were fed by the edge ports. The metallic sheets were treated as infinitely thin. The mesh was created through the default meshing settings.

The 60 GHz single feed linearly polarized patch array was simulated in CST using the transient solver based on the finite integration technique. An extra distance of one eighth of the free space wavelength was added between the bounding box using a perfectly matched layer boundary and the simulation model. The microstrip feedline of the array was fed by a waveguide port. The minimum number of mesh lines per free-space wavelength was set to 10.

The simulation of the standard gain horn was carried out using a simplified model with infinitely thin sheets of perfect electric conductor (PEC) in FEKO with the MoM full-wave solver.

The simulation time for these DUT model to converge were between 1 min (60 GHz Horn) to 4h (28 GHz mockup) on a 64 Gb 4.2 GHz i7-7700 machine.

3.2 Measurement Setup

All measurements were conducted with the setup mounted on a Newport RS 2000 optical table and were similar in both the measurement campaigns (28 GHz and 60 GHz), only the antennas, connectors and cables were changed. The amplitude and phase of the signal were measured using a probe connected to a Rohde & Schwarz ZVA 67 GHz. A custom-made Sony rectangular waveguide probe was utilized in the 28 GHz campaign and an RFspin OEWG WR15 probe in the 60 GHz campaign. The scan plane was realized using two THORLABS LTS300/M positioners combined with aluminum breadboards. This gives a maximum scan plane area of 30 cm×30 cm. The points in the scan plane were sampled on an 8 mm × 8 mm (4/5 λ) grid for the 28 GHz campaign and a 2 mm×2 mm (2/5 λ) grid for the 60 GHz campaign a view of other grid sizes and their impact can be viewed in Appendix D. The positioners and the VNA were controlled using a laptop and General Purpose Interface Bus (GPIB) connection. The DUT was mounted in a similar fashion and held stationary during the measurement and the distance between the DUT and probe scan plane were realized using said positioners. The alignment of the DUT and probe was done using the positioners and several cross laser units, achieving an accuracy of $\sim 50\,\mu$m. The cables were calibrated to their respective ends using an electrical calibration unit. The aperture was centered on a 30 cm × 23 cm metal sheet, which was mounted on a polymethyl methacrylate (PMMA) holder.

3.3 Specifications for the 28 GHz Measurements

The DUT for the measurements at 28 GHz, supplied by Sony Mobile, is seen in Fig. 2a where the mockup is mounted on absorbers and with one of its ports active (port 2). The mockup was secured firmly and special care was taken when changing the active port to not change the well specified position and further impact alignment. The distance between the probe scan plane and the DUT was 6 cm and

the scanned plane was a 28.8 cm × 28.8 cm plane sampled on a 8 mm × 8 mm grid. All four antennas on the DUT were measured, and for two different planes of the antenna.

The small aperture was manufactured using a laser milling machine. The aperture was illuminated using a SATIMO SGH2650 standard gain horn antenna. The distance between the aperture and the probe scan plane was 6 cm. The frequency band measured for both the aperture and the DUT was 26–30 GHz with 101 linearly spaced frequency points.

3.4 Specifications for the 60 GHz Measurements

The planar patch array antenna [5] used for the 60 GHz measurement was fed by a single port fixated on a custom 3D printed plastic holder, see Fig. 2c. The connector and transmission line were bent over a rounded edge of the custom made mount. This was done to reduce the impact of the connector in the measurement and to have a planar surface for the equivalent currents. The distance between the probe scan plane and the DUT was 2.5 cm and the scanned plane was a 10 cm × 10 cm plane sampled on a 2 mm × 2 mm grid.

The measurement of the Flann 25240−20 standard gain horn antenna was carried out on a 10 cm×10 cm plane distanced 50 mm away sampled on a 2 mm×2 mm grid.

The 60 GHz aperture was manufactured on a sheet of size, 30 cm × 23 cm. The aperture was illuminated using a Flann 25240 − 20 standard gain horn antenna. The illuminating horn antenna had a HXI HHPAV-222 power amplifier connected to it in order to get sufficient power through the aperture. The frequency band measured for both the aperture and the DUTs was 59 − 61 GHz with 101 linearly spaced frequency points.

4 Discussion

For the three different DUTs presented in this work, the measured and simulated power densities compare well in regions of high values. This can be observed in Figs. 3-5 and alternatively viewed from the difference between them, see Appendix B. The difference in the maximal spatial peak power density and the difference of the maximum spatially averaged power density, presented in Table 1, show similar quality. In this table 4 cm^2 was chosen as the averaging area and more areas are investigated in Appendix A.

For the 28 GHz mockup the results for plane 1, Fig. 3a, compare well, both in positioning and in shape, regardless of evaluation distance. Since the radiating area of the DUT—illustrated by the white lines in the figure—is narrow and stretches only a few wavelengths horizontally ($\approx$ 100 mm $\approx$ 10 λ at 28 GHz), the source surface can be discretized and evaluated numerically with high accuracy. The difference, to the corresponding simulated value, in the maximum spatial peak power density is reasonably low, 8-21 %, and for the difference in maximum spatially averaged power density that value is 10%-15%. The difference is low for close distances and increase

further away as the power density as the power density experience more spatial spread in the simulations than in the reconstructed fields, Fig. 3.

For plane 2, Fig. 3b, the position of the maximum spatial peak power density compare well between simulations and measurements. The field agrees best in the two upper quadrants and some minor disagreements are spotted in the bottom two. The reason for this is that only the top half part of the chassis, indicated by the white lines, is discretized and used as a source plane. If the entire chassis were to be used, substantial computational resources would be required for storing the necessary matrices and performing the matrix operations. Consequently, the current existing on the lower part of the chassis is not captured properly, and the corresponding radiated fields are not present in the reconstructed images. The maximum spatially averaged power density values are thus heavily affected due to the normalization procedure utilized creating this apparent large difference. The difference in maximum spatial peak power density is, as such, higher than that of plane 1, 23-67 %. The same is true for the difference in maximum spatially averaged power density, 17-30%. Note however that this drawback is preventable by utilizing additional computational resources.

The results for the 60 GHz patch antenna, Fig. 4, agree well between simulations and measurements. From the simulations it is observed that the transmission line, in the left part of the graphs, is apparent in the simulations but not observed to be as prominent in the measurements. The simulation model did not have the transmission line bent around a rounded edge as was done during the measurements, which in part might explain the results. Disregarding any effect stemming from the transmission line, the agreement is good; the same trends are observed and the symmetries are similar, as expected based on the geometry of the object. This is further seen by the fact that the difference in the maximum spatially averaged power density is very low 1-3%. However, the difference in the maximum spatial peak power density is interestingly much larger, 2-39 %. From studying the graphs in Fig. 4 we see that the simulated data have local high intensity regions near the patches of the array. These cannot be seen as clearly in the measured data, leading to a large difference point wise, in the peak power density, but not impacting the average power density in the region.

The results for the 60 GHz standard gain horn antenna, depicted in Fig. 5, compare well with a low difference of the maximal spatial peak power density, 0.7-7 % and low difference of the maximum spatially averaged power density 0.3-2%. By comparing the simulation to the synthetic data input and the measurement data input to the synthetic data input, the sources of inaccuracies can be isolated to the reconstruction technique and the quality of the retrieved field components, respectively. The power density along the horizontal line observed in the simulated results are not observed in the measurements and only partly in the synthetic data. This difference can be explained by having a finite measurement plane not capturing all radiated power, thus not reconstructing the side lobes fully. It is implicit that by capturing a larger fraction of the radiated power, either through measuring a more directive DUT or using a larger measurement plane (ideally an enclosing surface), the accuracy of the reconstructed fields would increase. The horn was simulated as

an infinitely thin PEC and most of the errors occur close to the device and below -20 dB in which the accuracy of the model can be questioned.

In general, for the data presented in Figs. 3-5 and in Table 1, the difference in maximum spatial peak power density between measurements and simulations is around 15 %, but varies depending on the specifics of the DUT. The difference in maximum spatially averaged power densities within 4 cm^2 region is around 2 % of the corresponding simulated value for the 60 GHz measurements and around 10-30 % for the 28 GHz mockup. This comparison adds confidence to the quality of the measurement technique, primarily when used to compare averaged values rather than peak values. However, the simulated results—due to the intricately manufactured designs and difficulty to model these accurately in commercial simulation software—should not be viewed as 'true' values but rather an approximate reference. For the 60 GHz horn and patch antenna the agreement is best at very close distances. There is a larger error at distances further away due to that the fields from the measurements do not spread as much as in the simulations, see Figs. 4 and 5. The same applies to the 28 GHz results. Furthermore, for the 28 GHz mockup plane 2 exhibits a larger error than plane 1; this is due to the fact that, for plane 2, the surface currents existing on the lower part of the chassis are not captured by the discretized source plane area.

The technique in this work has been demonstrated utilizing several devices at different frequencies and bandwidth, measured in planes 5λ to 10λ away and sampled on different grids with promising results. The technique should be most accurate for DUTs precisely aligned with the position of the aperture during calibration. However, in the case of the 28 GHz mockup, the presented results were that of the antenna furthest away from this origin, *i.e.* 3λ off center, yet the technique does not break down and gives promising results. A more elaborate study on the relationship between the phase center location of the DUT and the aperture position, as well as the effect of the quality of the chosen probe, is a consideration for future work.

The technique is experimentally straight forward to implement and from the indirect investigations of different parameters demonstrated in this work, it is indicated that the calibration works well for a wide array of setting and that an experimental accuracy of positioning is not mandatory as it is given through the calibration where an origin is fixated to that of the aperture position. Further work include exploring the limits of this method for a selection of parameters.

Throughout this paper, the DUTs have been linearly polarized antennas with an assumed low cross polarization. A single measurement of a DUT extracts a single field component from the registered voltage signal of the probe. Any field that is reconstructed via the technique described in this paper will thus be reliant on the information contained in a single measurement. However, two polarizations may be incorporated by conducting an additional measurement of the DUT with a modified orientation of the receiving probe and adding another polarization in the MoM code. Adding additional probes leads to a drastic improvement in measurement time as a scan currently takes between 40 min to 2 hours. Scanning with multiple probes or an array is interesting for future work as the technique should function without modification to the numerical implementation.

5 Conclusion

In this work, a measurement technique for RF EMF assessments of mm-wave 5G communication devices has been presented. The technique combines the well-known method of source reconstruction on a predefined surface representing the radiating aperture of an antenna, with an innovational calibration approach that utilizes a small aperture to calibrate both the measurement probe impact on the received signal, and the experimental setup in terms of the relative distance between the probe and the DUT. The accuracy in positioning obtained through anchoring the measurement setup to the position of the small aperture enables accurate reconstruction of the power density mere fractions of a wavelengths away from the DUT.

The measurement technique has been demonstrated on two mm-wave DUTs—specifically developed for 5G applications—operating at 28 GHz and 60 GHz respectively, and a standard gain horn as a benchmark case. The agreement between simulations and the reconstructed fields from measurement data is very good.

6 Acknowledgments

We thank Dr Ying Zhinong at Sony Mobile for valuable discussions and the use of the 28 GHz probe and mockup. Further, we wish to thank for the support from the Mobile and Wireless Forum, the GSM Association, and the Swedish Foundation for Strategic Research. We also thank Dr Alexander Bondarik for the use of the 60 GHz antenna and the corresponding simulation model.

Appendices

A Additional Results

In addition to $4\,\mathrm{cm}^2$ averaging region of the power densities presented Table 1, based on the results in Figs. 3-5, the result of $1\,\mathrm{cm}^2$, $2\,\mathrm{cm}^2$ and $3\,\mathrm{cm}^2$ can be seen in Table 2. The values presented in this table, and Table 1 is obtained through the following procedure. First the maximal value, y, of the convolution between a circular region of a certain area with the simulated power density at a given plane is recorded and the position of the circle saved. Then the corresponding value, x, is then computed for the measured power density. The difference is then computed through $|x-y|/y$.

Table 2: The relative difference between the measurement data set, x and the simulation data set, y for maximum spatially averaged power density. The averaging was carried out over a circular area of area $1/2/3\,\mathrm{cm}^2$. Each data set has been individually normalized to the same relative output power. The rows correspond to different data sets and the columns to different reconstruction distances.

	Relative difference of the maximum spatially averaged power density $:= \lvert x-y\rvert/y$			
	1 mm	5 mm	10 mm	20 mm
Horn (measured)	14/2/0.1 %	2/0.1/1 %	1/3/2 %	-
Horn (synthetic)	3/1/0.3 %	0.7/2/2 %	4/3/1 %	-
60 GHz Patch	5/2/0.5 %	2/0.3/0.1 %	4/2/1 %	-
28 GHz Plane 1	-	4/8/10 %	12/11/11 %	19/18/16 %
28 GHz Plane 2	-	46/40/37 %	40/37/34 %	26/28/27 %

B Supplementary Results

Another view of the data presented in Figs. 3-5 is to compute the difference between them as, $|10\log_{10}\{P_\mathrm{m}\} - 10\log_{10}\{P_\mathrm{s}\}|$, where m and s stands for measurements and simulations respectively. This is plotted in Fig. 6 and shown on a color scale spanning 40 dB. In these plots an unaveraged, point wise, comparison between the measurements and simulations is displayed.

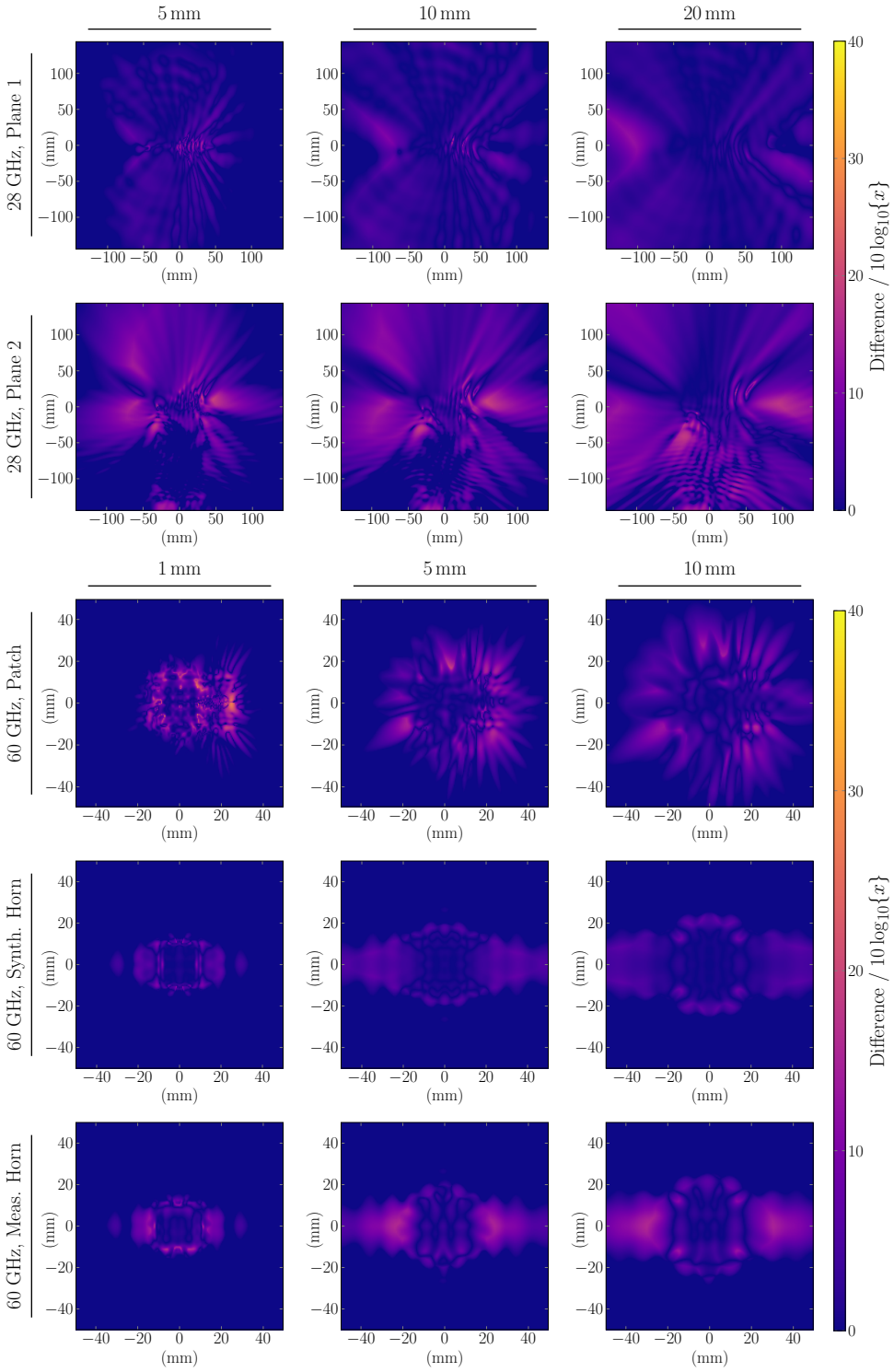

Figure 6: Difference between simulated and measured power density at different reconstruction distances, from the data in Fig. 3-5.

Yet another visualization is to take a horizontal and vertical cut of the figures presented in Figs. 3-5. This is shown in Fig. 7 for the 60 GHz measurements and in Fig. 8 for the 28 GHz measurements. In these plots the simulated data is represented

by solid lines and synthetic data is dashed. The different colors show different distance where green is the closest and blue the furthest. The cuts were chosen such that they both ran through the peak value.

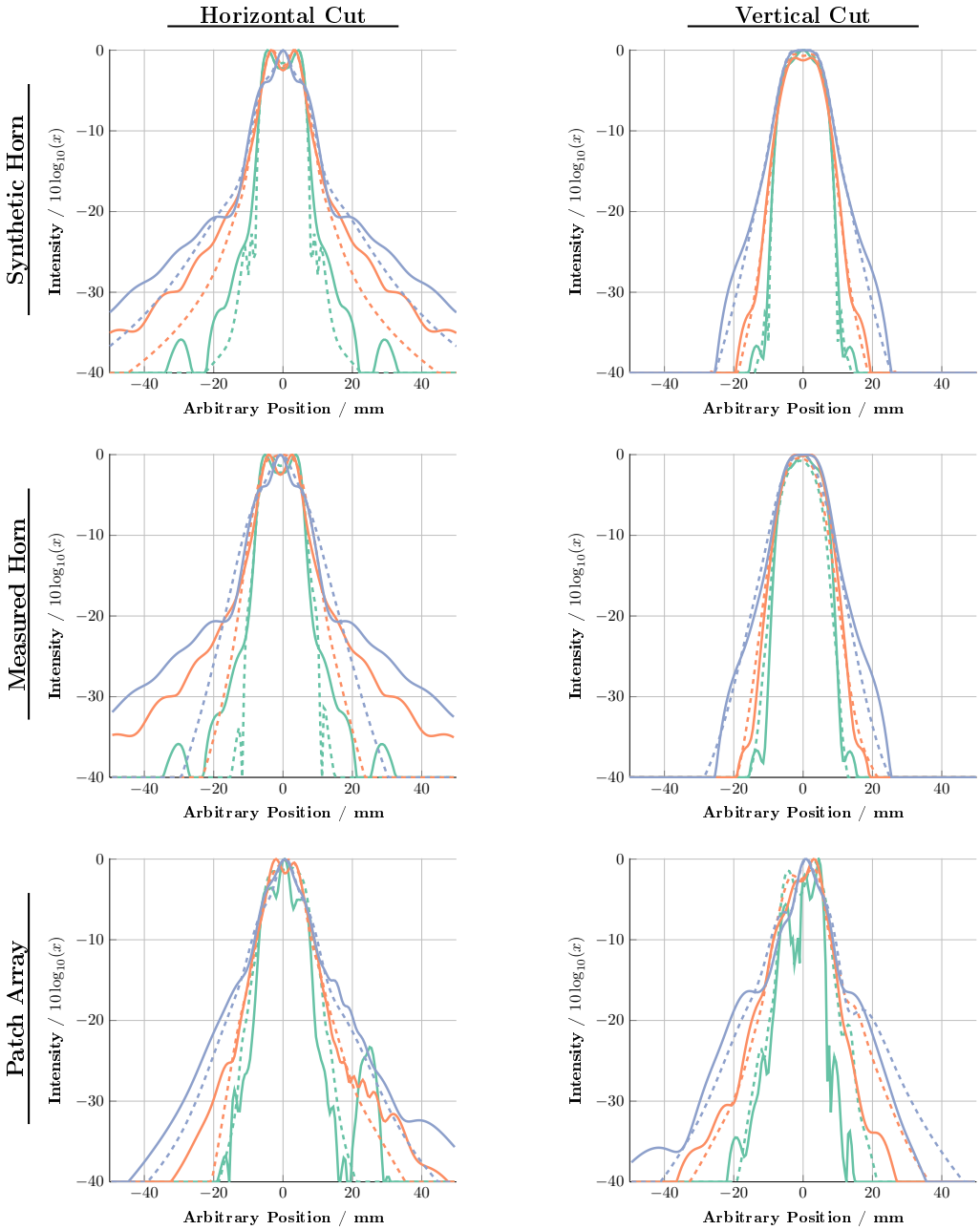

Figure 7: 60 GHz simulated, solid line, and reconstructed power density, dashed, for different two cuts through the peak value of Fig. 5 and Fig. 4. Three distances are displayed, 1 mm (green), 5 mm (orange) and 10 mm (blue).

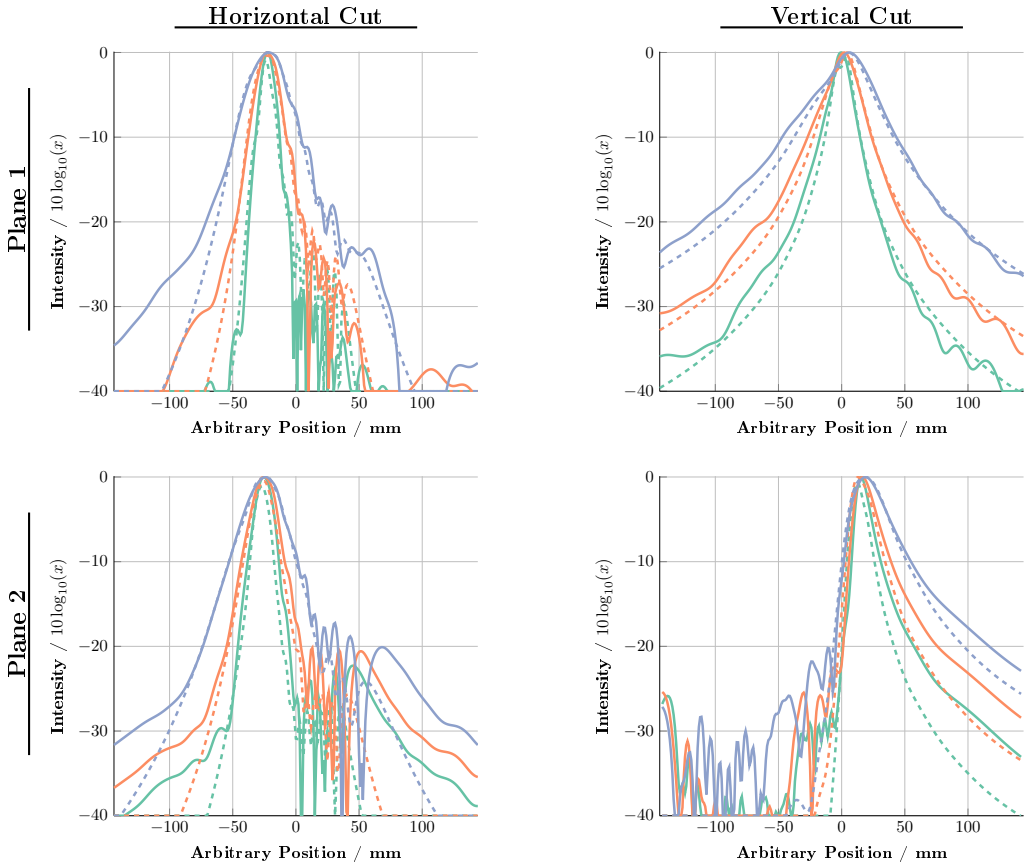

Figure 8: 28 GHz simulated, solid line, and reconstructed power density, dashed, for different two cuts through the peak value of Fig. 3. Three distances are displayed, 5 mm (green), 10 mm (orange) and 20 mm (blue).

C Truncation of Singular Values

An example of how the singular values look for the 28 GHz mockup phone is seen in Fig. 9. Here the singular values are plotted in a loglog scale. Different cuts of the singular values are shown by the red lines. The inset figures show the result for these different values of the tuning parameter, consequently including all singular values up to the corresponding red line.

As evident by Fig. 9 there is a large difference between a parameter choice of 0.5 and 0.001. However, those values should never be considered as the tuning parameter value. We choose a value around the knee of the plot [12]. Around the knee it can be seen that the solution is fairly stable, even when altering the cut off by a factor of 2. The graph as illustrated in Fig. 9 was similar for all cases throughout the work and a cutoff value of 0.1 was selected for all presented data.

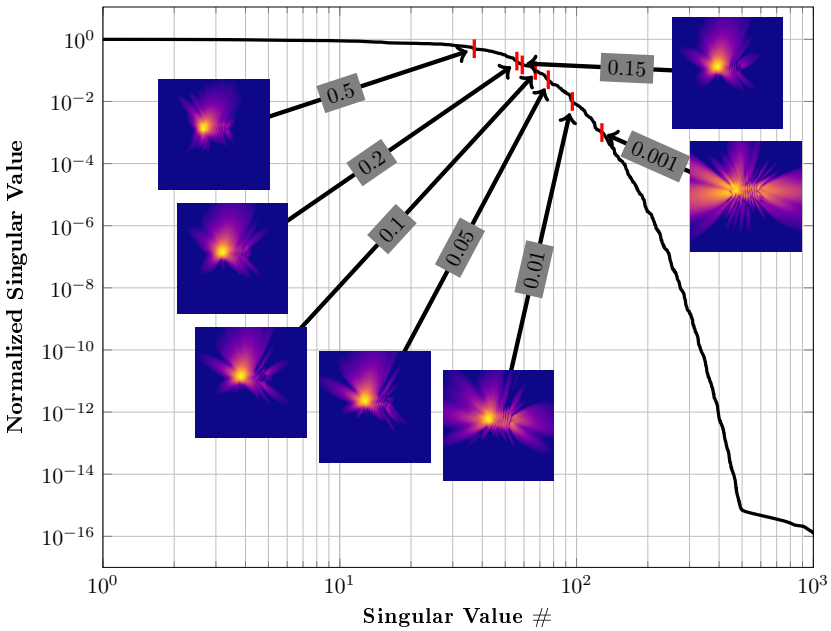

Figure 9: Singular values, normalized to the maximal value, of the matrix obtained in the 28 GHz mockup, plane 2, case. Inset figures display power density reconstruction result for different choices of tuning parameters, displayed in the grey boxes.

D Investigations of Measurement Parameters

In Fig. 10 the results of an investigation of bandwidth, B, as well as the frequency sampling δf, for one antenna on the 28 GHz mockup phone is shown. Each row corresponds to a certain change of bandwidth or frequency sampling; The first row is a reference measurement; For the second row the bandwidth is halved; The third row has double the frequency spacing; the fourth row shows both a doubling in frequency spacing and half bandwidth; the last row shows the situation where there is no time gating or processing of the measured signal at all before applying the technique presented in the manuscript. The different columns show the received signal in time domain for a measured point in the center of the scanned plane. The second column shows the reconstructed power density 5 mm away and the last column shows the difference between the reconstructed field in column two and the reference measurement, row 1 column 2, *e.g.* computed through $|10\cdot\log_{10}(P_{\mathrm{m}}) - 10\cdot\log_{10}(P_{\mathrm{s}})|$, where m stands for measurement and s for simulation. The graphs are all shown on a 40 dB color scale.

Further investigations into sampling and frequency was carried out and is presented in Fig. 11. The first column shows the original, fully sampled, plane and the second row, for each frequency, shows the difference between the fully sampled and the result given a reduced sampling. The difference is computed as discussed in $|10\log_{10}(P_{\mathrm{m}}) - 10\log_{10}(P_{\mathrm{m}})|$). The three different frequencies are 27, 28 and 29 GHz and the measurement is conducted on a scan plane sampled on a $4n/5\lambda$, $n = \{1, 2, 3, 4\}$ grid.

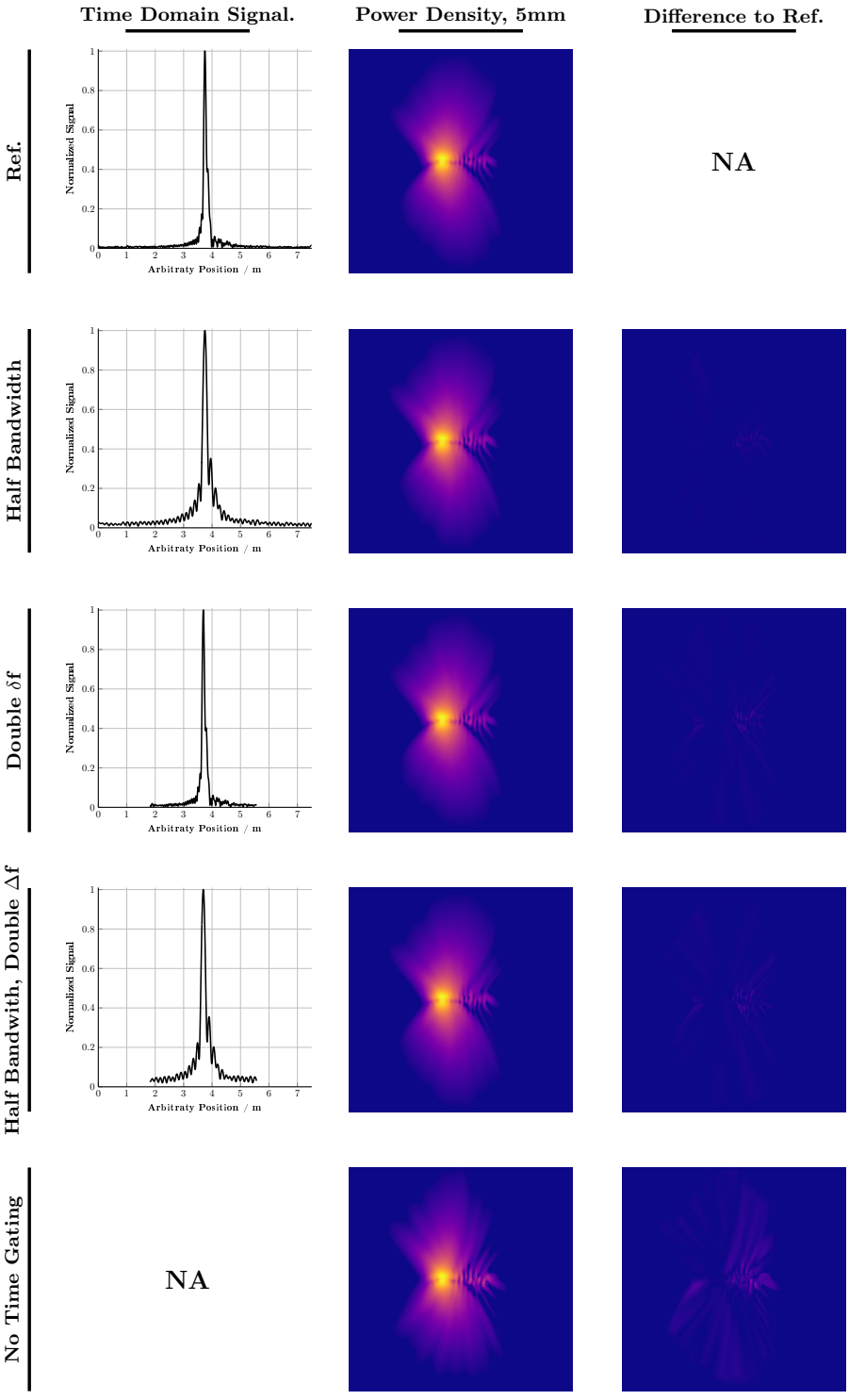

Figure 10: Reconstructed power density at 5 mm, column 2, for different measurement bandwidths and frequency sampling of a measurement of the 28 GHz mockup. Time domain signal in column 1 and difference to reference measurement in the third column.

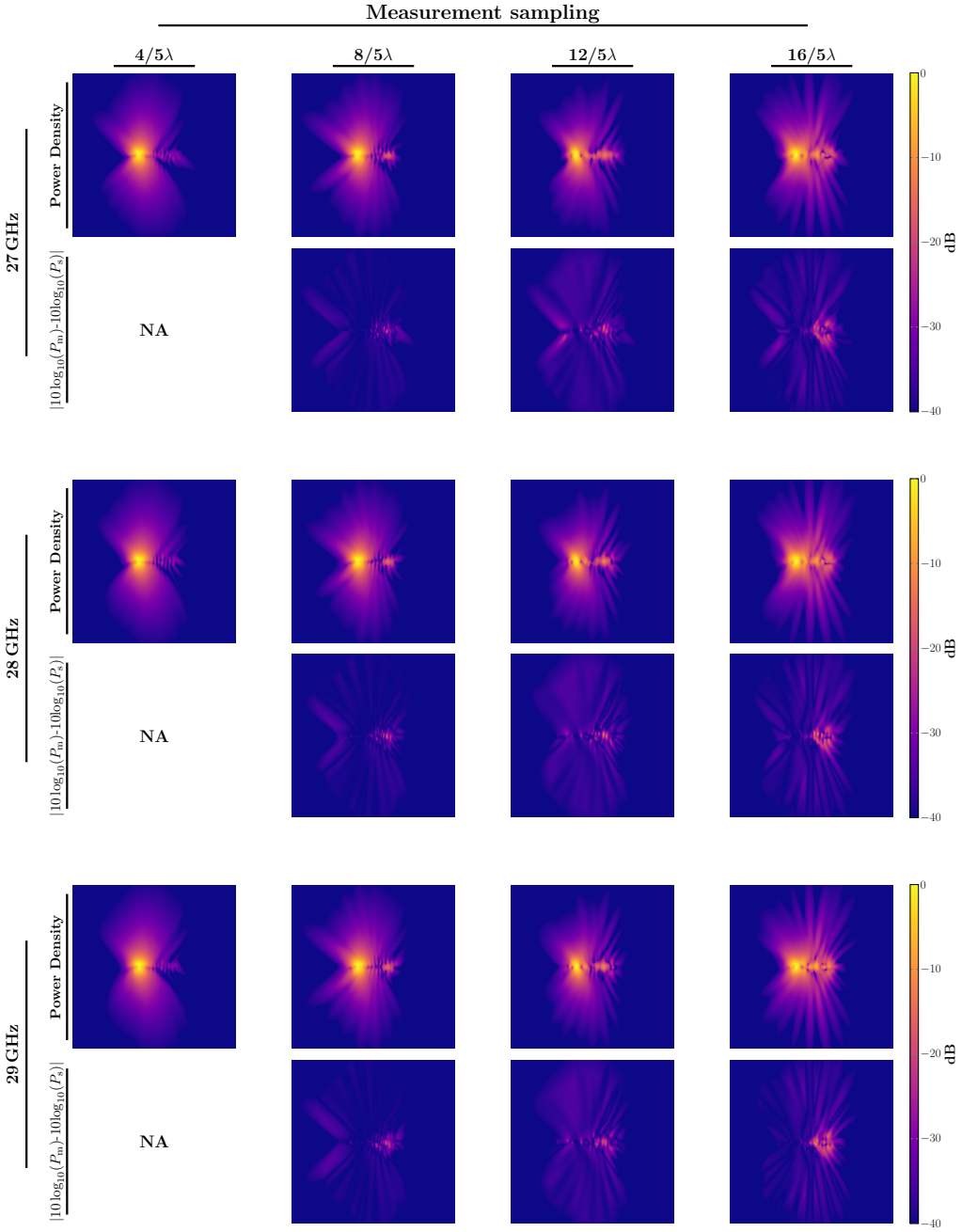

Figure 11: Reconstructed power density for three frequencies, rows, and four scan resolutions, columns. The difference between the reference, first column, and the other scan resolutions are seen in the second row of each frequency.

E Noise

In Fig. 12 the reconstruction for different values of Signal to Noise Ratio (SNR) is shown. This graph was generated by taking the measurement data, with an uncharacterized level of noise, and adding additional white Gaussian noise corresponding

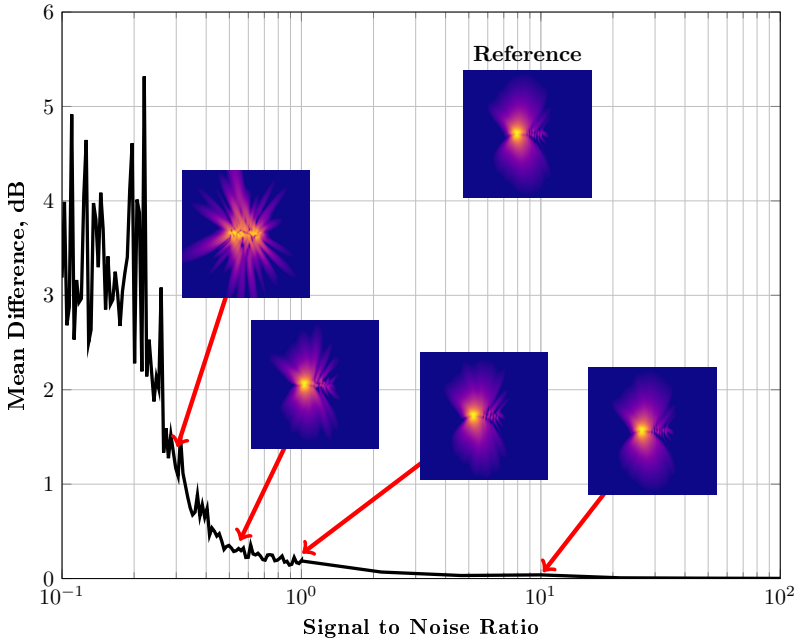

Figure 12: Mean Difference, in dB, between simulated and measured power density for different signal to noise ratios. The inset figures display the reconstructed power density at certain values of SNR and the reference with no additional noise.

to a certain SNR value. The value on the y-axis is computed as the mean value of the difference in dB, with the difference computed as $|10\log_{10}(P_{\mathrm{m}}) - 10\log_{10}(P_{\mathrm{m}})|$. The inset figures depict the power density for different values of SNR.

F Normalization

The reconstructed and simulated power densities are computed for a given plane with a given grid. This normalization procedure used for Table 1 is done by summing up the total power in the plane and then dividing each value in the grid with that sum. Thus, the total energy in the plane is normalized to 1. This is done to both simulations and the measurements before a comparison between them is made. Following is an example, consider a measurement, and subsequent reconstruction of the power density, P^{m}, of a DUT in plane, A. The total observed energy in this plane is then given by,

$$P^{\mathrm{m}}_{\mathrm{tot}} = \sum_{i,j} [P^{\mathrm{m}}]_{i,j} \mathrm{d}x\mathrm{d}y,$$

Here, $\{i, j\}$ are the grid points and $\mathrm{d}x$,$\mathrm{d}y$ is the discretization of the grid. The normalized power density, $P^{\mathrm{m}}_{\mathrm{norm}}$, using the normalization described is,

$$[P^{\mathrm{m}}_{\mathrm{norm}}]_{i,j} = \frac{[P^{\mathrm{m}}]_{i,j}}{P^{\mathrm{m}}_{\mathrm{tot}}},$$

A similar procedure is then followed for the simulated power.

References

[1] L. Alon, S. Gabriel, G. Y. Cho, R. Brown, and C. M. Deniz. "Prospects for millimeter-wave compliance measurement technologies [measurements corner]". *IEEE Antennas and Propagation Magazine* 59 (2) (2017): pp. 115–125.

[2] S. A. Altair Development S.A. (Pty) Ltd Stellenbosch. *FEKO, Field Computations Involving Bodies of Arbitrary Shape, Suite 7.0*. `https://www.feko.info/`, Retrieved: 24/11/2014. 2014.

[3] Y. Alvarez, F. Las-Heras, and M. R. Pino. "Reconstruction of equivalent currents distribution over arbitrary three-dimensional surfaces based on integral equation algorithms". *IEEE Trans. Antennas Propag.* 55 (12) (2007): pp. 3460–3468.

[4] J. G. van Bladel. "Electromagnetic Fields". Second Edition. IEEE Press, 2007.

[5] A. Bondarik and D. Sjöberg. "60 GHz microstrip antenna array on PTFE substrate". In: *Antennas and Propagation (EUCAP), 2012 6th European Conference on*. IEEE. 2012, pp. 1016–1018.

[6] W. C. Chew, M. S. Tong, and B. Hu. "Integral Equation Methods for Electromagnetic and Elastic Waves". Vol. 12. Morgan & Claypool, 2008.

[7] A. J. Devaney. "Mathematical foundations of imaging, tomography and wavefield inversion". Cambridge University Press, 2012.

[8] T. F. Eibert and C. H. Schmidt. "Multilevel fast multipole accelerated inverse equivalent current method employing Rao-Wilton-Glisson discretization of electric and magnetic surface currents". *IEEE Trans. Antennas Propag.* 57 (4) (2009): pp. 1178–1185.

[9] Ericsson. *5G Radio Access*. Tech. rep. Ericsson white paper, Ericsson AB, Stockholm, Sweden, 2016.

[10] FCC. *RF exposure: Order/NPRM issues. Technical Analysis Branch, Office of Engineering and Technology*. `https://transition.fcc.gov/oet/ea/presentations/files/oct18/5.1-TCB-RF-Exposure-OrderNPRM-Issues-MD.pdf`, Retrieved January, 2019. 2018.

[11] Flann Microwave. *Standard Gain Horns Series 240*. Flann Microwave Ltd. 2018.

[12] P. C. Hansen. "Discrete inverse problems: insight and algorithms". Vol. 7. Society for Industrial & Applied Mathematics, 2010.

[13] J. Helander and Z. Ying. *Stripline coupled antenna with periodic slots for wireless electronic devices*. U. S. Patent, no. 10,103,440. 2018.

[14] J. Helander, A. Ericsson, M. Gustafsson, T. Martin, D. Sjöberg, and C. Larsson. "Compressive sensing techniques for mm-wave nondestructive testing of composite panels". *IEEE Trans. Antennas Propag.* 65 (10) (2017): pp. 5523–5531.

[15] N. Heuveldop et al. *Ericsson mobility report*. Tech. rep. EAB-17 5964. Technol. Emerg. Bus., Ericsson AB, Stockholm, Sweden, 2017.

[16] ICNIRP. "Guidelines for limiting exposure to time-varying electric, magnetic, and electromagnetic fields (up to 300 GHz)". *Health phys* 74 (4) (1998): pp. 494–522.

[17] IEC. *IEC TR 63170 ED1: Measurement procedure for the evaluation of power density related to human exposure to radio frequency fields from wireless communication devices operating between 6 GHz and 100 GHz, Tech. Rep., International Electrotechnical Commission,* tech. rep. 2018.

[18] D. Kerns. "Correction of near-field antenna measurements made with an arbitrary but known measuring antenna". *Electron. Lett.* 6 (11) (1970): pp. 346–347.

[19] G. Kristensson. "Scattering of Electromagnetic Waves by Obstacles". SciTech Publishing, an imprint of the IET, 2016.

[20] K. Persson and M. Gustafsson. "Reconstruction of equivalent currents using a near-field data transformation – with radome applications". *Prog. Electromagn. Res.* 54 (2005): pp. 179–198.

[21] S. Pfeifer, E. Carrasco, P. Crespo-Valero, E. Neufeld, S. Kühn, T. Samaras, A. Christ, M. H. Capstick, and N. Kuster. "Total field reconstruction in the near field using pseudo-vector E-field measurements". *IEEE Trans. Electromagn. Compat.* 61 (2 2019): pp. 476–486.

[22] S. M. Rao. "Time Domain Electromagnetics". Academic Press, 1999.

[23] SPEAG. *EUmmWVx / 5G ProbeE-Field mm-Wave Probe for General Near-Field Measurements.* Schmid & Partner Engineering AG, Zurich, Switzerland, [Online] `https://speag.swiss/products/dasy6/probes/new-eummwvx-vector-e-probe/`, Retrieved: Jan. 2019.

[24] R. Vallauri, G. Bertin, B. Piovano, and P. Gianola. "Electromagnetic field zones around an antenna for human exposure assessment: evaluation of the human exposure to EMFs." *IEEE Antennas and Propagation Magazine* 57 (5) (2015): pp. 53–63.

[25] A. D. Yaghjian. "An overview of near-field antenna measurements". *IEEE Trans. Antennas Propag.* 34 (1) (1986): pp. 30–45.